

Experimental investigation of matrix permeability of gas shales

Rob Heller, John Vermilyen, and Mark Zoback

ABSTRACT

Predicting long-term production from gas shale reservoirs has been a major challenge for the petroleum industry. To better understand how production profiles are likely to evolve with time, we have conducted laboratory experiments examining the effects of confining stress and pore pressure on permeability. Experiments were conducted on intact core samples from the Barnett, Eagle Ford, Marcellus, and Montney shale reservoirs. The methodology used to measure permeability allows us to separate the reduction of permeability with depletion (because of the resultant increase in effective confining stress) and the increase in permeability associated with Knudsen diffusion and molecular slippage (also known as Klinkenberg) effects at very low pore pressure. By separating these effects, we are able to estimate the relative contribution of both Darcy and diffusive fluxes to total flow in depleted reservoirs. Our data show that the effective permeability of the rock is significantly enhanced at very low pore pressures (<1000 psi [<6.9 MPa]) because of the slippage effects. We use the magnitude of the Klinkenberg effect to estimate the effective aperture of the flow paths within the samples and compare these estimates to scanning electron microscopy image observations. Our results suggest effective flow paths to be on the order from tens of nanometers in most samples to 100–200 nm, in a relatively high-permeability Eagle Ford sample. Finally, to gain insight on the scale dependence of permeability measurements, the same core plugs were crushed, and permeability was again measured at the particle scale using the so-called Gas Research Institute method. The results show much lower permeability than the intact core samples, with very little correlation to the measurements on the larger scale cores.

Copyright ©2014. The American Association of Petroleum Geologists. All rights reserved.

Manuscript received February 11, 2013; revised manuscript received June 10, 2013; revised manuscript received July 29, 2013; revised manuscript received August 15, 2013; revised manuscript received August 19, 2013; accepted September 23, 2013.

DOI: 10.1306/09231313023

AUTHORS

ROB HELLER ~ *Department of Geophysics, Stanford University, Stanford, California 94305; rjheller@stanford.edu*

Rob Heller earned his Ph.D. in geophysics from Stanford University in 2013. His thesis was titled "Multiscale Investigation of Fluid Flow in Gas Shales", and his adviser was Dr. Mark Zoback. He earned his M.S. degree from Stanford University in environmental engineering in 2008, and a B.S. degree from Columbia University in 2007.

JOHN VERMYLEN ~ *Department of Geophysics, Stanford University, Stanford, California 94305; john.vermylen@gmail.com*

John Vermilyen earned his Ph.D. in geophysics from Stanford University in 2011. His thesis was titled Geomechanical Studies of the Barnett Shale, and his adviser was Mark Zoback. Vermilyen earned his M.S. degree in geophysics from Stanford University in 2008, and his B.S. degree from Princeton University in 2005.

MARK ZOBACK ~ *Department of Geophysics, Stanford University, Stanford, California 94305; zoback@stanford.edu*

Mark Zoback is the Benjamin M. Page Professor of geophysics at Stanford University. His research focuses on in-situ stress, fault mechanics, and reservoir geomechanics with an emphasis of shale gas, tight gas, and tight oil production. He is the author of a textbook entitled *Reservoir Geomechanics*, published in 2007 by Cambridge University Press. He holds a Ph.D. and an M.S. degree in geophysics from Stanford University.

ACKNOWLEDGEMENTS

We gratefully acknowledge financial support from the Department of Energy (Grant DE-FE-0004731), the Research Partnership to Secure Energy for America, and the Stanford Rock and Borehole Geophysics consortium. In addition, we thank ConocoPhillips and BP for providing samples for us to work with. We also thank Terrilyn Olsen for her review of our article. The AAPG Editor thanks Senior Associate Editor Terrilyn M. Olsen and the following reviewer for their work on this paper: Farzan Javapour.

INTRODUCTION

A common characteristic of all shale gas reservoirs is their extremely low intrinsic permeability. To produce gas at any significant rate, the rock must first be hydraulically fractured to expose additional surface area and provide greater contact with the reservoir. Although fracture properties (both natural and induced) may dominate reservoir performance early on in the life of a well, it is the matrix properties that control how a well will perform over longer periods of time. This study focuses on the fluid-flow properties of the matrix.

Understanding in-situ matrix permeability and how it evolves with depletion is a major challenge to gas shale reservoir characterization and is essential for accurate production forecasting. As such, many research efforts to date have been aimed at this topic. Several of these studies have involved measuring the impacts of stress on matrix permeability. For example, Bustin et al. (2008) measured the sensitivity of permeability to confining pressure at a single pore pressure. In contrast, Kang et al. (2011) measured sensitivity of permeability to pore pressure at a single confining pressure. Kwon et al. (2001) measured intact plug permeability over a range of both pore and confining pressures. Other efforts have aimed at profiling permeability along a well log or length of core. For example, Yang and Aplin (2010) developed a permeability-porosity relationship for mudstones using a large data set consisting of both measured permeability values and estimates based on clay content and pore-size distribution, but did not investigate confining and pore-pressure effects. Clarkson et al. (2012) developed a method for profiling permeability along a shale core sample, which was calibrated using pulse permeability measurements on plugs. Finally, several studies have involved efforts to perform rapid permeability estimation on crushed shale samples (Luffel and Guidry, 1989; Luffel and Hopkins, 1993; Egermann et al., 2003; Cui et al., 2009). The disadvantages of performing measurements on crushed samples include potentially eliminating larger scale features (such as microcracks) and the inability to perform measurements at reservoir conditions or measure how permeability evolves during

production. In this work, we draw upon many of these previous studies and methodologies in an effort to further understand matrix permeability in organic-rich gas shales and their sensitivity to both effective confining pressure and pore pressure.

As gas is produced and reservoir pressure decreases, two different processes alter the permeability of the rock. These processes can be categorized as stress effects and flow regime effects. Stress effects are relatively straightforward: as pore pressure goes down, the matrix feels an increase in effective stress (defined here as the difference between hydrostatic confining pressure and pore pressure), which narrows pore throats and lowers the permeability of the rock. This effect is well known, and variation of permeability with effective stress has been studied fairly extensively for sandstones and carbonates (Warpinski and Teufel, 1992; Al-Wardy and Zimmerman, 2004; Ghabezloo et al., 2009). As noted above, such measurements are much more limitedly available for organic-rich shales.

The second phenomenon affecting permeability is a flow regime effect and is less intuitive. As discussed in more detail below, transport at low gas pressure and in small pores is a mixture of Darcy flow (in which the flow rate is proportional to the pressure gradient) and diffusion flow (in which molecular transport exists along the walls of the flow channels). This is sometimes referred to as slippage flow, in reference to molecules slipping past one another, and was initially studied by Klinkenberg (1941). These processes result in an increase in transport relative to pure Darcy flow, which manifests itself as an apparent increase in the permeability of the rock.

In this study, we investigate stress and flow regime effects in the laboratory. An overview of this study is as follows:

1. Using established pulse-decay methods, we measured permeability sensitivity to effective stress in several shale samples over a range of confining pressures and pore pressures and fit each data set with an empirical effective stress law.
2. Using a testing methodology that allowed us to isolate stress effects from flow regime (slip flow) effects in the laboratory, we determined the extent

to which slip flow becomes important during depletion.

3. We also measure permeability on crushed samples from the same core plugs for comparison.

Finally, using the results from above, we present a working conceptual model for flow through that matrix of gas shales as pressure depletes.

BACKGROUND

Stress-Dependent Permeability

Many physical properties of porous rocks (permeability, volumetric strain, porosity, etc.) vary as a function of confining pressure and pore pressure according to an effective pressure law. This is known as Terzaghi's principle, and the Terzaghi effective stress (sometimes called simple or nominal effective stress) is defined as follows:

$$\sigma_{\text{Terzaghi}} = C_P - P_P \quad (1)$$

where C_P is the confining pressure and P_P is the pore pressure. This simple effective stress law (as it will be referred to hereafter) is frequently modified to include a coefficient affecting the pore-pressure term so that the relative importance of confining pressure and pore pressure can be described in a single parameter. When describing how volumetric strain varies with effective stress, the appropriate coefficient is defined as the Biot coefficient, α (Nur and Byerlee, 1971).

Many efforts have been made to describe how permeability depends on effective stress (Zoback and Byerlee, 1975; Walls and Nur, 1979; Kwon et al., 2001). The objective of these experiments has been to fit all permeability data to an effective stress law such that given a confining pressure and pore-pressure combination, the permeability of a rock can be predicted. The effective stress law takes on the following form:

$$\sigma_{\text{eff}} = C_P - \chi P_P \quad (2)$$

where σ_{eff} is true effective stress and χ is the effective stress coefficient for permeability. Thus, χ determines the relative sensitivity of permeability

to changes in confining pressure and pore pressure. Most rocks have been shown to have $\chi \leq 1$, indicating that the rock is more sensitive to changes in confining pressure than pore pressure. However, a handful of studies of clay-bearing sandstones have found χ to be greater than 1, implying that changes in pore pressure have a larger impact on permeability than confining pressure (Zoback and Byerlee, 1975; Walls and Nur, 1979). A simple conceptual model for this observation, developed by Zoback and Byerlee, 1975, suggests that fluid flows through a pore surrounded by a relatively soft compressible matrix, whereas the external stresses are supported by the stiff granular framework of the rock. Therefore, if pore pressure and confining pressure were to increase by the same amount, for example, the compressible nature of the flow paths relative to the incompressible frame allows the change in pore pressure to have a greater effect on the pore-size aperture than the external stress, increasing the overall permeability of the rock.

In contrast to observations of $\chi > 1$ in high-clay sandstones, Kwon et al. (2001) measured $\chi \sim 1$ in very weak, high-clay Wilcox shale samples from the Gulf of Mexico. Since Kwon's investigation, other studies have measured the sensitivity of gas shale matrix permeability at a single pore pressure (Bustin et al., 2008) or at a single confining pressure (Kang et al., 2011). However, there have been no previous studies of shale matrix permeability over a range of effective stresses and pore pressures.

Flow Regime Effects on Permeability

Expanding on the introduction above, flow in gas shales (and similarly tight rocks) is described by a combination of transport mechanisms acting at different scales (Javadpour et al., 2007; Wang and Reed, 2009; Freeman et al., 2011). These include the following:

1. Surface diffusion of molecules adsorbed to kerogen and clay surfaces;
2. Knudsen diffusion and slip flow in micro-, meso-, and some macropores; and
3. Darcy flow in macropores.

It is common to denote transitions between these various flow regimes using the dimensionless Knudsen number, defined as

$$\text{Kn} = \frac{\lambda}{d_p} \quad (3)$$

where d_p is the diameter of the pore and λ is the mean free path of a molecule moving through it, calculated as

$$\lambda = \frac{K_{\text{Boltz}} T}{\sqrt{2} \pi d_m^2 P} \quad (4)$$

where K_{Boltz} is the Boltzmann constant, T is the temperature, d_m is the molecular diameter, and P is the pressure. The molecular mean free path becomes larger as pressure (gas density) decreases. The relationship between the Knudsen number, pore width, and pressure is displayed in Figure 1. At very small Knudsen numbers ($\text{Kn} < 0.01$), the mean free path of gas molecules is negligible relative to the pore width, and the continuum assumption (Darcy flow) is valid. At very large Knudsen numbers ($\text{Kn} > 10$), gas molecules collide more frequently with pore walls than with each other, and thus, the continuum assumption becomes invalid, and flow rate and pressure drop are no longer accurately predicted using Darcy's law. Under these conditions, molecules no longer move as a viscous fluid but instead move independently of one another (i.e., gas composition has no significance), colliding back and forth between flow boundaries as they travel through the pore (Knudsen flow). Within the intermediate region ($0.01 < \text{Kn} < 10$) between these two extremes, neither free molecular nor continuum flow models are valid by themselves, and flow is a combination of the two mechanisms. This intermediate zone is further subdivided into slip and transition flow regimes, with the distinction between the two being the relative amounts of free molecular and Darcy flow contributing to total flow. Table 1 summarizes these four types of flow regimes and the driving forces associated with each.

Flow in gas shales lies mostly within the Darcy, slip, and transition flow regimes. Under these conditions, flow has been mostly modeled as a weighted combination of pure Poiseuille (Darcy) and Knudsen flow. Within the petroleum engineering literature, Klinkenberg (1941) was the first to do this.

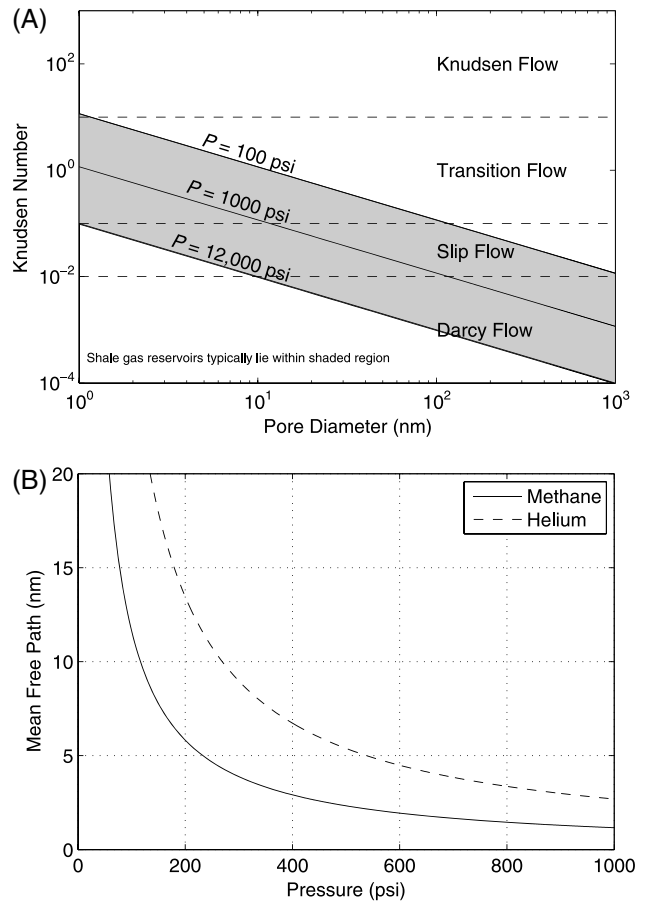


Figure 1. (A) Dimensionless Knudsen number versus pore diameter (nm) for methane at 100°C. Shaded region indicates pressures and pore sizes typical of gas shale reservoirs. Most of the gas shale reservoirs lie within the slip and transition and Darcy flow regimes given their pore-size distributions and reservoir pressures. (B) Mean free path of methane and helium versus pressure. The lower the pressure, the lower the gas density is and the larger the mean free path. The mean free path of helium is approximately double that of methane because of its smaller molecular size. The mean free path of both increases significantly at pressures below approximately 500 psi (3.4 MPa).

Klinkenberg's primary objective was to develop a way of estimating liquid permeability from measurements made with gas. In contrast to gas, liquids are sufficiently dense such that the mean free path is almost always negligible relative to the pore width, and slippage effects are absent. Therefore, to estimate liquid permeability from gas measurements, the magnitude of the slippage effect must be quantified and corrected for. He suggested measuring permeability at several pressures and plotting the resulting permeability measurements versus inverse pressure

Table 1. Summary of Flow Regimes, Corresponding Knudsen Number and Driving Force Behind Each Flux*

| Flow Regime | Knudsen Number | Driving Force |
|---------------------------------|--------------------------|---|
| Knudsen/free molecule flow | $\text{Kn} > 10$ | Total concentration gradient and molecular weight |
| Transition flow | $0.1 < \text{Kn} < 10$ | Mostly Knudsen flow with some Darcy flow |
| Slip flow | $0.01 < \text{Kn} < 0.1$ | Mostly Darcy flow with some Knudsen flow |
| Continuum/Darcy/Poiseuille flow | $0.01 > \text{Kn}$ | Total pressure gradient |

*Mineralogy, kerogen analyses, and other sample characteristics for samples used in this analysis. Pressure and pore sizes typical of most gas shale reservoirs place it within the slip, transition, and Darcy flow regimes.

($1/P$). Theory predicts a linear trend, with a y-intercept (infinite pressure) equal to the liquid permeability of the rock and the slope reflecting the changing magnitude of the mean free path with pressure relative to the effective pore width (Knudsen number). The equation he derives is as follows:

$$k_a = k_\infty \left(1 + \frac{K_b}{P} \right) \quad (5)$$

where k_a is the apparent permeability (permeability measured with gas), k_∞ is the permeability at infinite pressure (liquid permeability), K_b is the Klinkenberg parameter, and \bar{P} is the mean flowing pressure across a sample. Klinkenberg cared mainly about straightforwardly obtaining liquid permeability, k_∞ , while measuring permeability with gas. In the context of gas shales (with the exception of liquid plays) the parameter K_b is of more importance because it tells us the extent to which permeability will change as a function of pressure caused by slippage.

METHODOLOGY

Plug Permeability Measurement

All measurements were made using helium as the test gas. This was done primarily to avoid the potentially significant effects of adsorption and/or associated swelling that might impact permeability

(Cui et al., 2009; Kowalczyk et al., 2010). Sample preparation included cutting, grinding, drying, and prestressing. Sample plugs were initially cut to a length of approximately 1–1.5 in. (2.5–3.81 cm), and size was cut down if permeability proved too low for measurements to be completed in a reasonable amount of time. The ends of each plug were ground until flat and subsequently placed in a vacuum oven at 45°C until constant mass was achieved to remove any water and/or residual hydrocarbons from the core. The temperature was chosen so as to be above the boiling point of water in near vacuum conditions, but not so high as to remove clay-bound water and alter the clay properties. Finally, the sample was loaded into the pressure vessel where it was prestressed for a period of 48–72 hr at an effective stress 25% greater than that which it would experience during the experiment. The purpose of this prestressing is to remove any inelastic deformation prior to beginning experiments. In addition to this prestressing, measurement repeatability was carefully monitored.

A schematic of the hydrostatic permeability system used for plug permeability measurements is shown in Figure 2. The sample is wedged between two floating plugs attached to pore lines inside a Viton jacket. Confining pressure is controlled manually using the high-pressure generator shown on the far right of Figure 2. Confining pressure is measured using a Heise DXD pressure transducer accurate to $\pm 0.1\%$ up to 10,000 psi (68.9 MPa). Pore pressure is controlled by a Quizix QX-6000 pump, equipped with two pistons capable of multiple operating modes including constant pressure, constant flow rate, and a variety of paired operating modes. The pump is capable of reaching a pressure of 6000 psi (41 MPa)

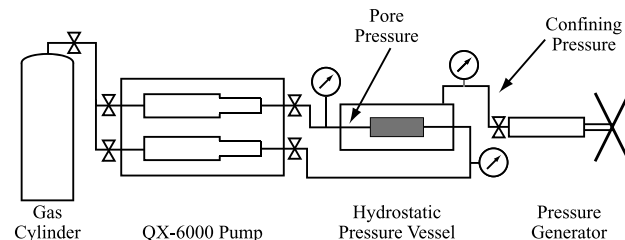


Figure 2. Simplified schematic of hydrostatic permeability system. Gas flows from one end of the rock sample to the other using the Quizix pump. The entire apparatus is placed inside of an insulated chamber, and temperature is controlled using a heat lamp with a feedback system.

and measuring pressure to an accuracy of $\pm 0.01\%$. All flow rates were measured via the Quizix system, capable of measuring flow rates as low as 0.001 mL/min, accurate to within $\pm 0.1\%$ of the set flow rate. Temperature within both the upstream and downstream pore lines as well as the confining pressure lines is measured with thermocouples. To maintain temperature stability, a custom heat control system was built using a heat lamp and a feedback algorithm implemented via LabVIEW™ (laboratory virtual instrument engineering workbench). All data were recorded using LabVIEW as well.

Depending on the permeability of the sample, either a steady-state Darcy flow method or a pressure pulse decay method was employed. Our system is capable of accurate Darcy flow measurements to approximately 1 μd for a 1.5-in. (3.81-cm) sample. For samples of lower permeability, equilibrium was not reachable in a reasonable amount of time using steady-state methods, and the pressure pulse approach was used instead. Of the six samples discussed in this article (described below), three samples were permeable enough for the Darcy flow method (Barnett 27, Eagle Ford 127, and Montney). The pressure pulse method was used for the three other samples (Barnett 31, Marcellus, and Eagle Ford 174).

The pressure pulse technique was first developed by Brace et al. (1968) to measure permeability of granite. The principle is to create a dynamically changing flow across the sample and then fit the resulting pressure curves to a flow model, thus determining permeability. In our case, we stepped the pressure on the upstream side by only 50 psi (0.34 MPa) to minimize the impact of a nonuniform effective stress (and thus, a nonuniform permeability) along the length of the sample. Although it is typical to increase the upstream pressure by a certain initial amount and then allow the upstream pressure to decline as the downstream rises, we set up our experiments with a constant pressure on the upstream side, creating an effective infinite reservoir volume (Zoback and Byerlee, 1975). This was done primarily to compensate for any gas leakage on the upstream side of our system.

An example of the downstream pressure recorded during a pulse-permeability test is shown in

Figure 3A. When the logarithm of the difference in pressure between the upstream and downstream sides is plotted versus time (Figure 3B), the decay clearly follows a linear trend. This line can be fit by the following equation (after Brace et al., 1968):

$$\Delta P(t) = \Delta P_0 e^{-\alpha t} \quad (6)$$

$$\alpha = \frac{kA}{\beta V_{\text{down}} L \mu} \quad (7)$$

where α is the decay exponent (the slope of the line on a plot of $\ln(\Delta P)$ versus time), $\Delta P(t)$ is the difference in pressure between the upstream and downstream sides at time t , ΔP_0 is the difference in pressure between upstream and downstream at time $t = 0$, β is the compressibility of the gas, V_{down} is the volume of the downstream reservoir, L is the length of the sample, A is the cross sectional area of

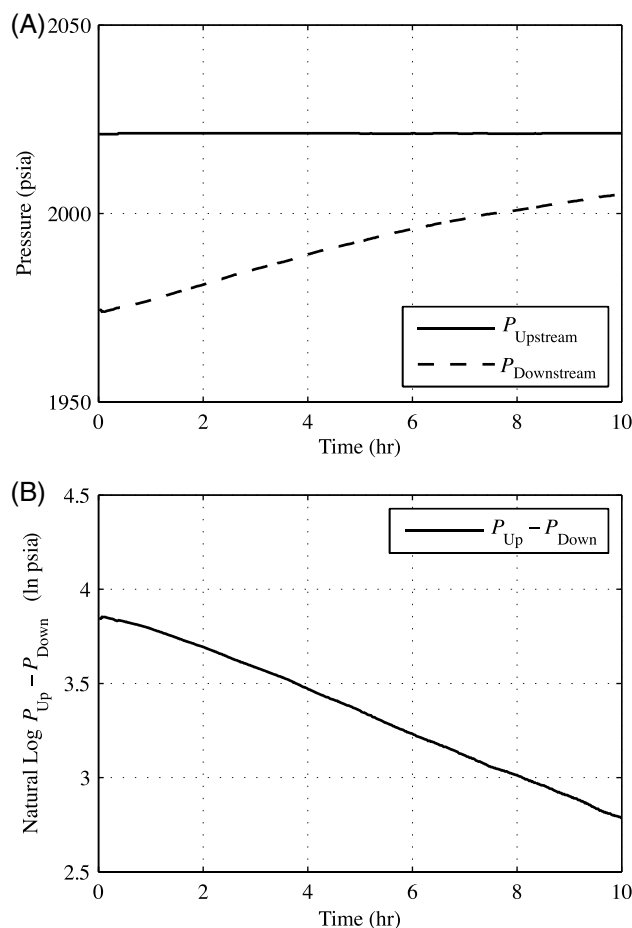


Figure 3. Pulse permeability example, showing the upstream and downstream pressure curves (A) and the logarithmic decay of the difference in pressure between the two reservoirs (B).

the sample, and μ is the viscosity of the fluid flowing through the sample.

To independently test the effects of effective stress, confining pressure, and pore pressure on permeability, it is necessary to measure the permeability over a wide range of P_p and C_p values. An example of the procedure is shown in Figure 4. At each of several pore-pressure steps, the sample is subjected to incrementally increasing confining pressures, and permeability is measured at each increment. Confining pressure is then decreased in the same increments, and permeability is again measured to monitor for repeatability. Following this sequence, pore pressure is increased, and the process is repeated up until the last pore pressure of interest (typically 4000 psi [27.6 MPa]).

To calculate the effective stress parameter for permeability, we use the ratio of slope method following Kwon et al. (2001) using the following equation:

$$\chi = \left(- \frac{\partial \log k / \partial P_p}{\partial \log k / \partial C_p} \right) \quad (8)$$

The change in permeability with change in pore pressure at a given confining pressure is divided by the change in permeability with change in confining pressure at a given pore pressure. This ratio defines the relative sensitivity of permeability to changes in pore and confining pressures. The use of the

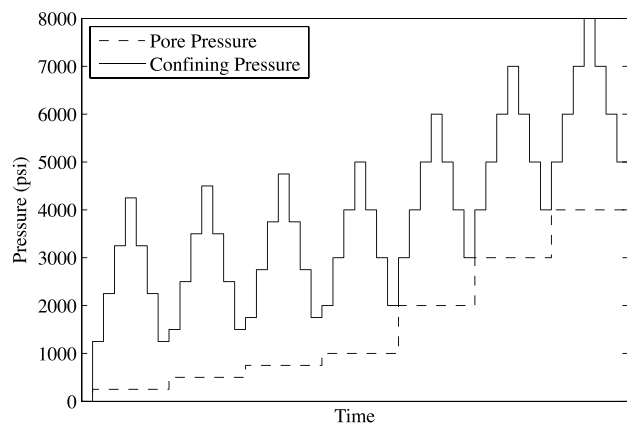


Figure 4. Confining pressure and pore-pressure steps during permeability testing. A long hold for equilibrium exists after each pore-pressure change. Tests are conducted with increasing effective stress and decreasing effective stress to monitor for hysteresis affects. A typical suite of measurements as shown in this figure takes approximately 30 days to complete.

logarithm of permeability is based purely on empirical fitting of the permeability decline as effective stress increases.

Although it is common to terminate measurements once $\Delta P(t)$ reaches approximately 30% of ΔP_0 (one-third the way to equilibrium), we allowed each step to proceed nearly to equilibrium to aid in leak rate characterization (see the Discussion section for further elaboration on leak detection). On average, this took approximately 24 hr. A full suite of confining pressure and pore-pressure combinations (as shown in Figure 4) took approximately 30 days to complete for a single sample.

A methodology for separating stress and flow regime effects on permeability will be presented in the next section using our experimental data. However, once this is accomplished, we can create standard Klinkenberg-style plots that can be used to estimate the effective aperture of the flow paths (Soeder, 1988). Suppose we assume that the total mass flow is the sum of the viscous flow plus some empirical constant times the Knudsen flow (Klinkenberg made a similar assumption). In addition, we assume the pore geometry to be slit-shaped based on observations of scanning electron microscopy (SEM) images. By modeling the viscous flux using the Poiseuille equation and combining this with the Knudsen flow and Klinkenberg equations, we can derive the following:

$$w = \frac{16c\mu}{K_b} \left(\frac{2RT}{\pi M} \right) \quad (9)$$

where w is slit width, c is an empirical constant, μ is the viscosity, R is the gas constant, T is the temperature, M is the molar mass, and K_b is the Klinkenberg constant. This provides a direct linkage between the empirical Klinkenberg constant and the effective pore aperture (full derivation presented in Appendix 1).

Crushed Permeability Measurements

Shale permeability is frequently measured on crushed shale sample as opposed to plugs because of the length of time required to make accurate measurements on such low-permeability rock (Luffel and

Guidry, 1989; Luffel and Hopkins, 1993; Egermann et al., 2003). However, many benefits of measuring permeability on intact core plugs exist as opposed to crushed core, including straightforward and established methods for interpreting data, sampling a large (and perhaps more representative) volume of rock, and the ability to test the influence of confining stress on permeability. Given our experimental objectives, we chose to perform our experiments on intact core plugs. However, crushed permeability measurements were additionally performed on several of the samples for comparison.

Once plug permeability measurements were complete, several core samples were subsequently crushed to a particle size of 1000–2000 μm and again placed in a vacuum oven at 45°C until constant mass was observed, implying that moisture had been removed. All crushed permeabilities measured were made on these chips inside a dual-chamber pressure apparatus. A schematic of this simple setup is shown in Figure 5.

The setup consists of a reference cell and sample cell, placed inside of a temperature-controlled oil bath capable of maintaining a constant temperature to $\pm 0.05^\circ\text{C}$. The volumes of both cells are adjustable to minimize dead volume and allow measurements to be made on varying amounts of sample without sacrificing sensitivity. The crushed sample was placed inside the sample cell, and the entire system was vacuumed to remove air. The valve separating the reference and sample cells was then closed, and the reference cell filled with helium to a pressure of about 150 psi (1 MPa). After pressure and

temperature stabilization was reached, this gas was allowed to expand into the sample cell. The dead volume within the lines and between the particles is filled immediately, and the pressure subsequently decays as gas permeates the shale particles. Equilibrium was reached after approximately 10 min or less. The pressure vs. time data leading up to equilibrium can then be used to estimate permeability, as first outlined by the Gas Research Institute (Luffel and Guidry, 1989) and later elaborated on by other authors (Luffel and Hopkins, 1993; Egermann et al., 2003; Profice et al., 2011). In this study, we interpret the pressure decay curves in the means outlined by Cui et al. (2009).

SAMPLE DESCRIPTION

In this article, results will be presented from two Barnett, two Eagle Ford, one Marcellus, and one Montney shale sample. The Barnett Shale is a Mississippian-age shale located in the Forth Worth Basin in north central Texas. The Eagle Ford Shale is a Late Cretaceous-age shale located in south Texas. The Montney Shale is an Early Triassic-age shale, located within the Western Canada Sedimentary Basin in British Columbia and Alberta.

With the exception of the Marcellus plug, all samples were oriented horizontally (sample axis oriented parallel to the surface of the Earth) such that the direction of flow is parallel to the bedding. The Marcellus was a vertical sample (sample axis oriented perpendicular to the surface of the earth); thus, flow was perpendicular to bedding. The mineralogy of the samples is shown in Figure 6, and a table with mineralogy and other sample information is included in Appendix 2. Mineralogy varies significantly from sample to sample, particularly the amount of quartz, carbonate, and clay. Both Barnett samples contained a high amount of quartz, whereas the Eagle Ford samples were dominated by carbonates and the Marcellus by clay. The Montney sample comprises a relatively even mixture of quartz, carbonate, clay, and feldspar.

In addition to mineralogy, three of the samples contained visible anomalies worth noting. Both Barnett 27 and Eagle Ford 127 samples contained calcite streaks that extended across the width and length

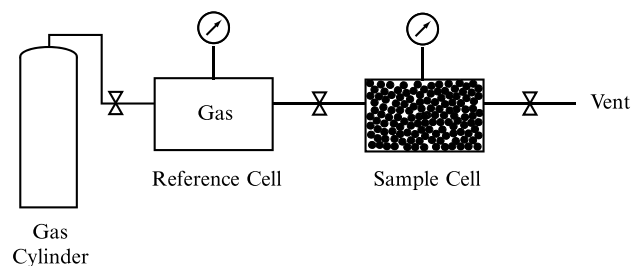


Figure 5. Schematic of system used for crushed permeability measurements. Both the reference and sample cells are placed inside of a temperature-controlled oil bath for stability. The volumes of both cells are adjustable using aluminum spacers to accommodate varying sample sizes without sacrificing measurement sensitivity.

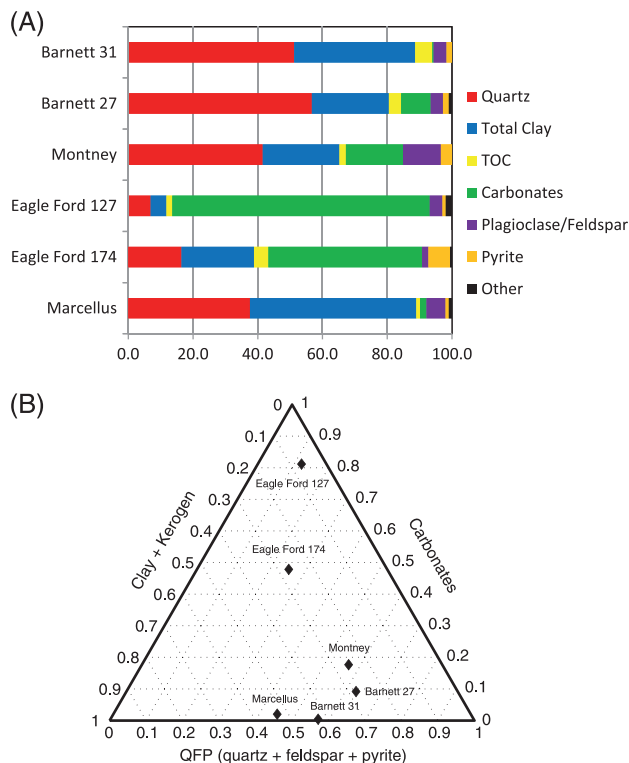


Figure 6. Mineralogy of samples included in this study (A). Ternary diagram representation of sample composition (B). Mineralogy varies significantly from sample to sample, particularly the amount of quartz, carbonate, and clay. Both Barnett samples contained a high amount of quartz, whereas the Eagle Ford samples were dominated by carbonates and the Marcellus by clay. The Montney sample comprised a relatively even mixture of quartz, carbonate, clay, and feldspar.

of the samples. The Montney sample contained a very minor crack (visible only when wet) oriented along its axis. Both the calcite streaks and crack enhanced permeability significantly, as will be described in the results section.

RESULTS

Plug Permeability Measurements

For all six samples studied, permeability was measured at pore pressures from 1000 to 4000 psi (6.9 to 27.6 MPa), confining pressures from 2000 to 8000 psi (13.8 to 55 MPa), and simple effective stresses ranging from 1000 to 4000 psi (6.9 to 27.6 MPa). These data were fit to an effective stress law. Of those six samples, three were chosen for additional permeability measurements at pore pressures

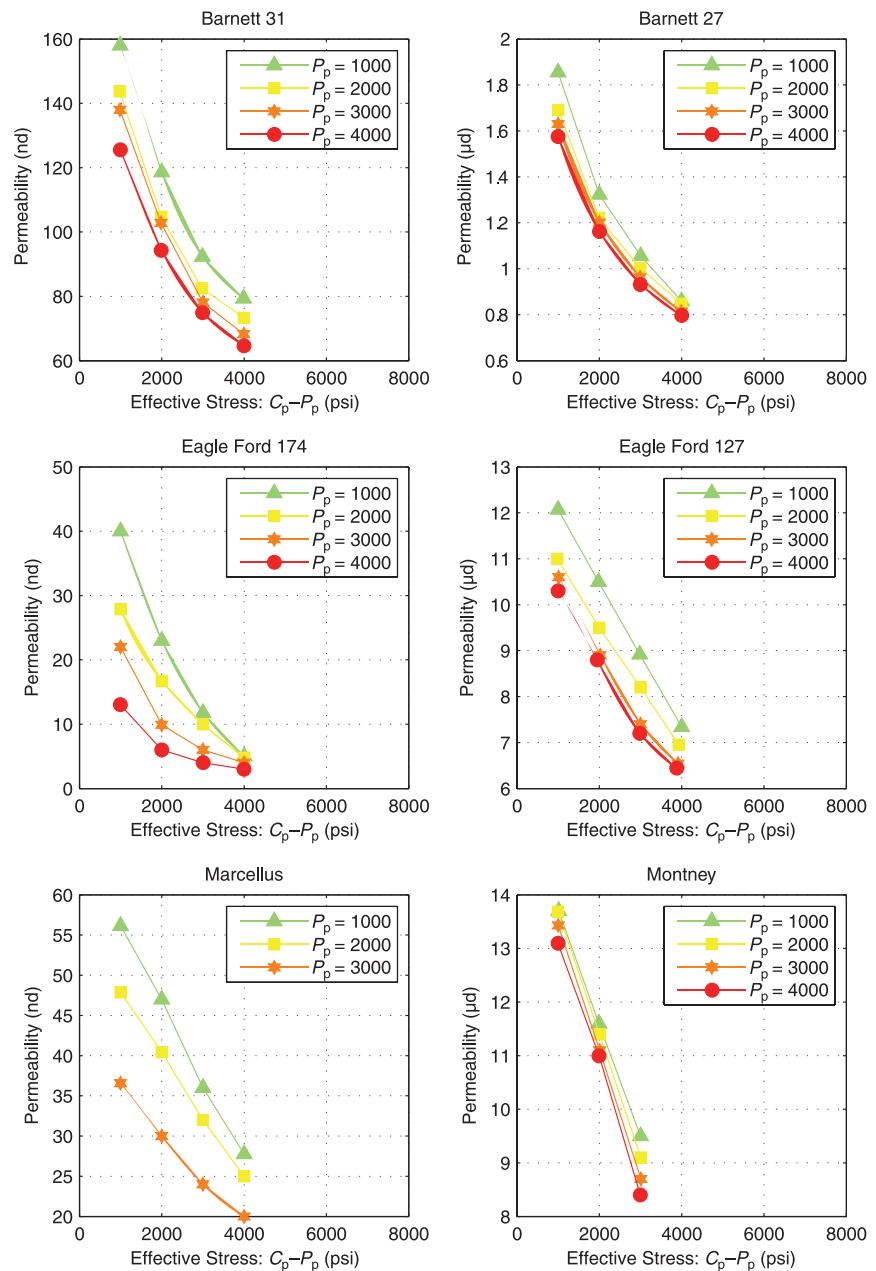
below 1000 psi (6.9 MPa). The results for the high pore-pressure data (all six samples) will be presented first, followed by a more in-depth look at the rocks for which low-pressure permeability measurements were also made.

Permeability as a function of simple effective stress ($C_p - P_p$) is shown for all six samples in Figure 7 at different pore pressures. Several features are worth pointing out. First, note the scale difference for the Barnett 27, Eagle Ford 127, and Montney samples (microdarcy as opposed to nanodarcy) and recall that each of these relatively high-permeability core plugs contained an anomalous throughgoing feature. Both the Barnett 27 and Eagle Ford 127 samples contained a carbonate layer extending through the core plugs. We believe these carbonate layers are highly permeable relative to the rest of the shale matrix, resulting in a larger than typical plug permeability value in these two samples. In addition, recall that the Montney sample contained what appeared to be a very minor crack oriented along its axis, which seems to have enhanced permeability. Finally, notice that for each sample, permeability varies as a function of simple effective stress ($C_p - P_p$) in a similar way, allowing for a single function to be fit to the whole data set.

The data for each rock were fit to a unique permeability effective stress law as described previously. These results are presented in Figure 8. In all cases, χ was found to be less than 1, indicating that the rocks are more sensitive to changes in confining pressure than changes in pore pressure. Noting that permeability as a function of modified effective stress forms a trend enables us to attribute all permeability variation observed (for $P_p > 1000$ psi [6.9 MPa] thus far) to effective stress effects.

As previously mentioned, three of the six samples were chosen for further characterization at lower pore pressures ($P_p < 1000$ psi [6.9 MPa]). A typical permeability sample (Eagle Ford 174), a high-permeability sample (Eagle Ford 127), and a vertical sample (Marcellus) were selected for variation. Permeability versus effective stress is plotted on the left in Figure 9 using the same effective stress law (same χ) previously found to fit the high-pressure data. It is apparent in this figure that the measurements made at low pore pressure deviate from the trend fit by

Figure 7. Permeability versus simple effective stress ($C_p - P_p$). Note that permeability units for samples Barnett 27, Eagle Ford 127, and Montney samples (right column) are in microdarcys; all other samples are in the nanodarcy range.



the high pore-pressure data. We attribute this permeability enhancement (relative to what one would predict given the effective stress) to slippage (i.e., Klinkenberg) effects, and we proceed to investigate how permeability varies as a function of pore pressure because of non-stress-related (Klinkenberg) effects. We select several values of true effective stress (indicated in Figure 9 by the black dashed lines) and create Klinkenberg plots for each by selecting points of intersection with the pore-pressure trend. The results are shown in the right half of Figure 9.

Several aspects of these Klinkenberg plots are worth pointing out. First, note the increase in the Klinkenberg constant (K_b) with increasing effective stress for each rock. This increase in K_b essentially represents an increase in gas slippage with increasing effective stress. This observation is intuitively reasonable, given that one would expect an increase in effective stress to narrow flow paths, thereby increasing the Knudsen number and the contribution from slip flow. It is also worthwhile to compare the magnitude of K_b between samples. Both the Eagle Ford 174

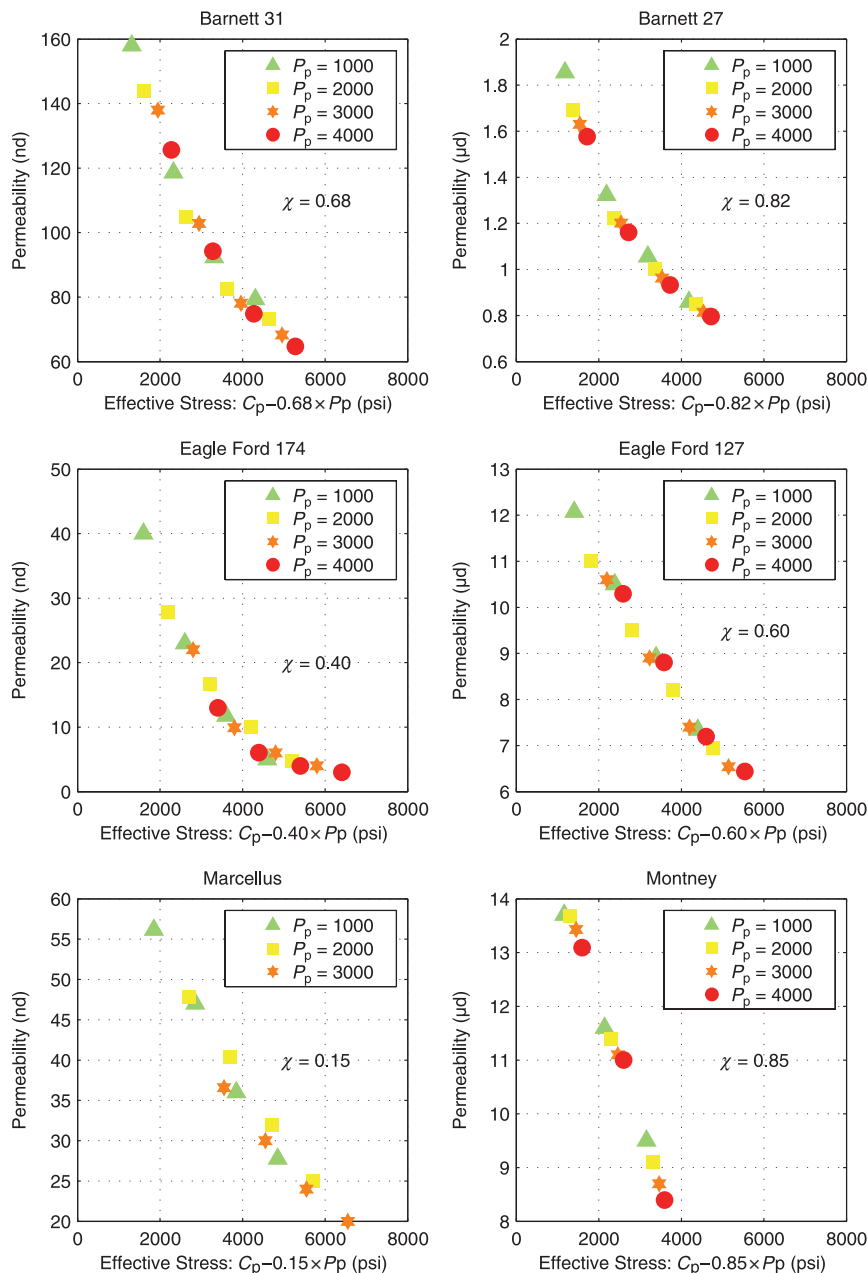


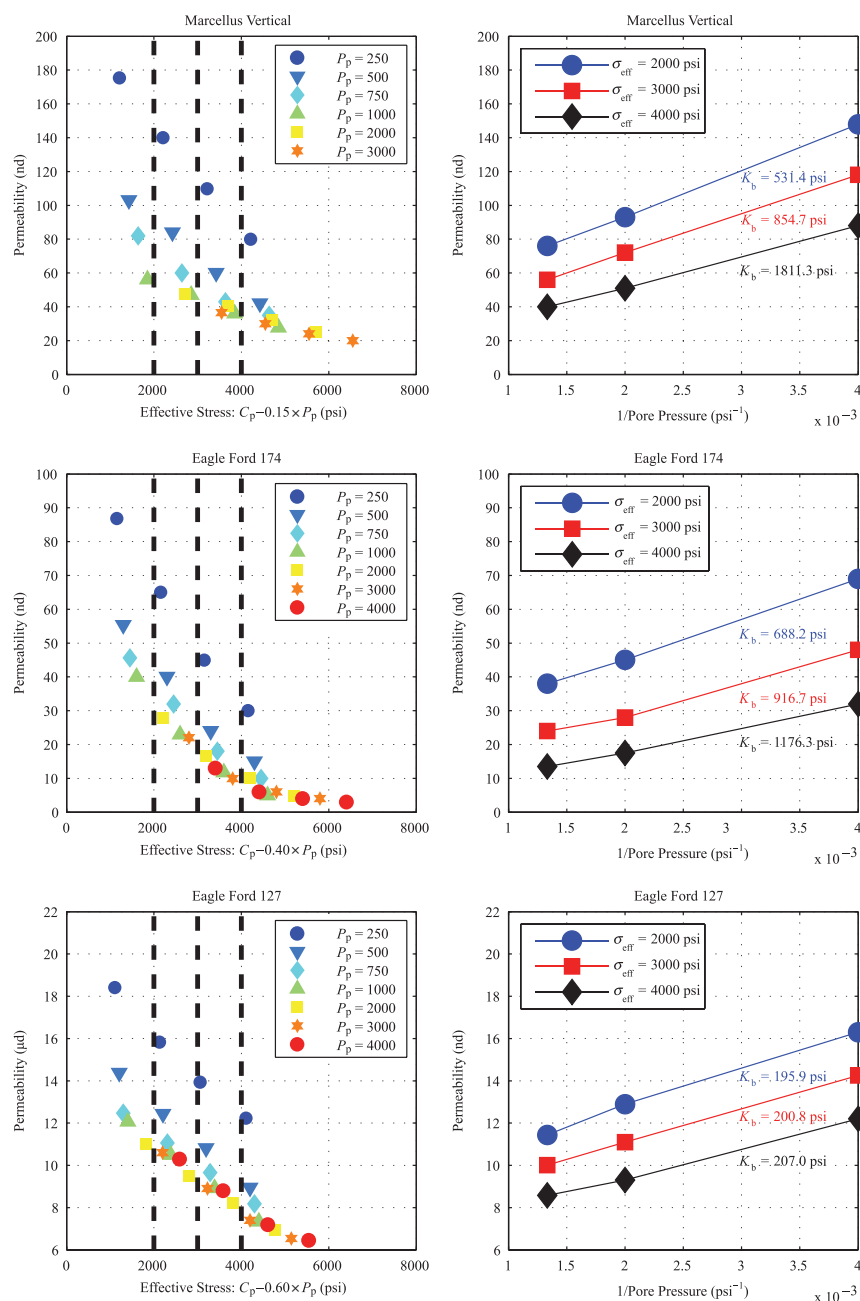
Figure 8. Permeability versus modified effective stress after data were fit to the effect stress law for each sample. In all cases, χ was found to be less than 1, indicating that the rocks are more sensitive to changes in confining pressure than changes in pore pressure. Noting that permeability as a function of modified effective stress forms a trend enables us to attribute all permeability variation observed (for $P_p > 1000$ psi [6.9 MPa] thus far) to effective stress effects.

and Marcellus samples are characterized as having a similar permeability, as well as similar contributions from slip flow as evidenced by the similar K_b values. This contrasts with the higher permeability Eagle Ford 127 sample, which has a lower K_b and, thus, a smaller overall contribution of slip flow to total flow. The overall contribution of slip flow to total flow in these samples will be further considered in the discussion section.

With Klinkenberg parameters established for each sample, we are now able to use equation 9 to calculate the effective size of the flow paths. Moreover,

because we have also determined how K_b varies with effective stress for each rock, we can estimate how the effective size of the flow paths varies with effective stress as well. These results are presented in Figure 10. Our calculations suggest that the effective pore size varies moderately with effective stress (about 5% in the case of Eagle Ford 127, factor of 2 in the case of Marcellus, and a factor of about 5 in the case of Eagle Ford 174). Although many assumptions went into these estimates (slit-shaped pores in particular), the results seem plausible based on the apertures of pore sizes commonly observed in SEM

Figure 9. Left: permeability versus modified effective stress with low pore-pressure data. Note the deviation from the high pore-pressure trend by the low pore-pressure points. Black dashed lines indicate effective stress isolines used for generating Klinkenberg plots by selecting their intersection with the permeability trend for several pore pressures ($P_p = 250, 500, \text{ and } 750 \text{ psi}$ [1.7, 3.4, and 5.1 MPa]). Right: standard Klinkenberg plots (permeability versus $1/P_p$). Permeability points were selected for true effective stress values of 2000, 3000, and 4000 psi (13.8, 20.7, and 27.6 MPa). Notice the increase in K_b value (slope divided by intercept) with increasing effective stress.



photos in the shale gas literature (Loucks et al., 2009; Curtis et al., 2010).

Crushed Permeability Measurements

Of the six core plugs, four were chosen for crushed permeability measurements at particle sizes of 1000–2000 μm . As previously described, the experiments were performed by expanding gas from a reference cell into a separate chamber containing the shale particles. Fractional uptake (defined as the fraction of

gas initially within the reference cell that has entered the shale particles) is plotted as a function of time in Figure 11. Permeability is approximately proportional to the amount of time required to reach equilibrium (when all intraparticle porosity has been filled). The magnitude of the fractional uptake (height of curve on the y-axis) at equilibrium is simply dependent on the porosity within the particles.

The data displayed in the fractional uptake versus time curves were interpreted following Cui et al. (2009), and lower and upper bounds on permeability

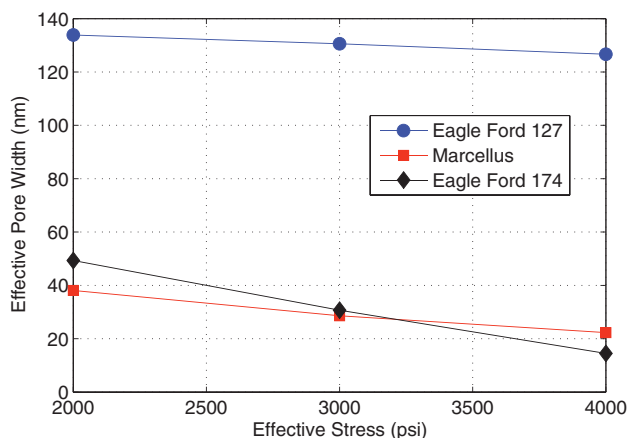


Figure 10. Effective pore width versus true effective stress, as estimated for the Klinkenberg parameter (K_b). Our calculations suggest that the effective pore size varies moderately with effective stress. Despite having to make several assumptions to arrive at these estimates, the results seem plausible based on the apertures of pore sizes commonly observed in SEM photos in the gas shale literature.

were estimated. The results are displayed in Figure 12. We calculate the permeability at this scale to be within the narrow range of about 1 to 10 nd. Because these measurements were made on the same samples as the plug measurements, we directly compare the calculated permeability values using the two different approaches and sample sizes in Figure 13. Note the large difference between permeability at the two different scales, with permeability at the plug scale being much higher than that at

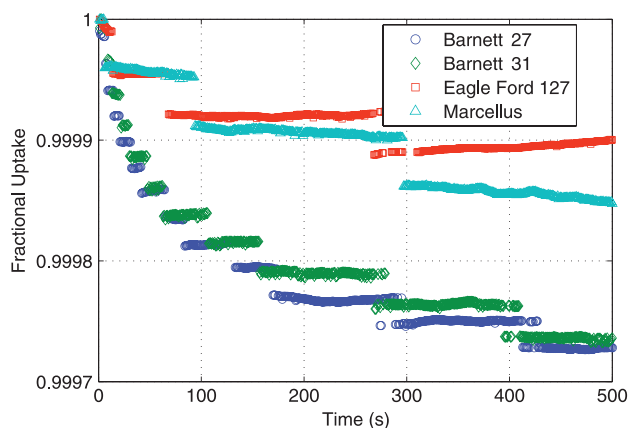


Figure 11. Fractional uptake (defined as the fraction of gas initially within the reference cell that has entered the shale particles) versus time. In this study, we interpret these pressure decay curves as outlined by Cui et al. (2009). Permeability is approximately proportional to the amount of time required to reach equilibrium.

the crushed particle scale. This suggests that much less heterogeneity exists at smaller scales than at larger scales, where microcracks and other features (such as carbonate layers) could enhance permeability. Moreover, we observe no systematic trend between plug and crushed permeability measurements. A discrepancy in permeability between the two different scales and lack of an obvious trend relating the two were also reported by Sinha et al. (2012).

SOURCES OF ERROR

Any investigation of permeability in such low permeability and complex formations would not be complete without discussing some of the potential sources of error. We begin this section by discussing general sources of error relevant to both plug and crushed measurements and follow that by addressing additional challenges specific to each approach.

General Error Discussion

An important consideration with regard to both plug and crushed permeability experiments is that we have performed all flow measurements using helium as opposed to methane. As previously discussed, with a smaller molecular diameter (helium has a diameter of 0.25 nm, whereas methane is 0.38 nm), helium has a larger mean free path compared to methane at a given pressure. Thus, the contribution of slip flow is enhanced relative to methane. In addition, as an adsorbing gas, the flow of methane may be impeded by the presence of an adsorbed layer. Such a complex combination of physics poses a major experimental challenge, particularly in the context of materials with flow paths as intricate as gas shales.

Another potentially significant detail worth discussing is the presence of residual oil in our samples. As mentioned, our samples were dried in a vacuum oven at 45°C prior to all experiments. Although effective at removing residual water, these conditions are insufficient to remove heavier hydrocarbons that may be trapped within the samples. Despite only one of our samples being conclusively within the gas window, very little reported oil production from

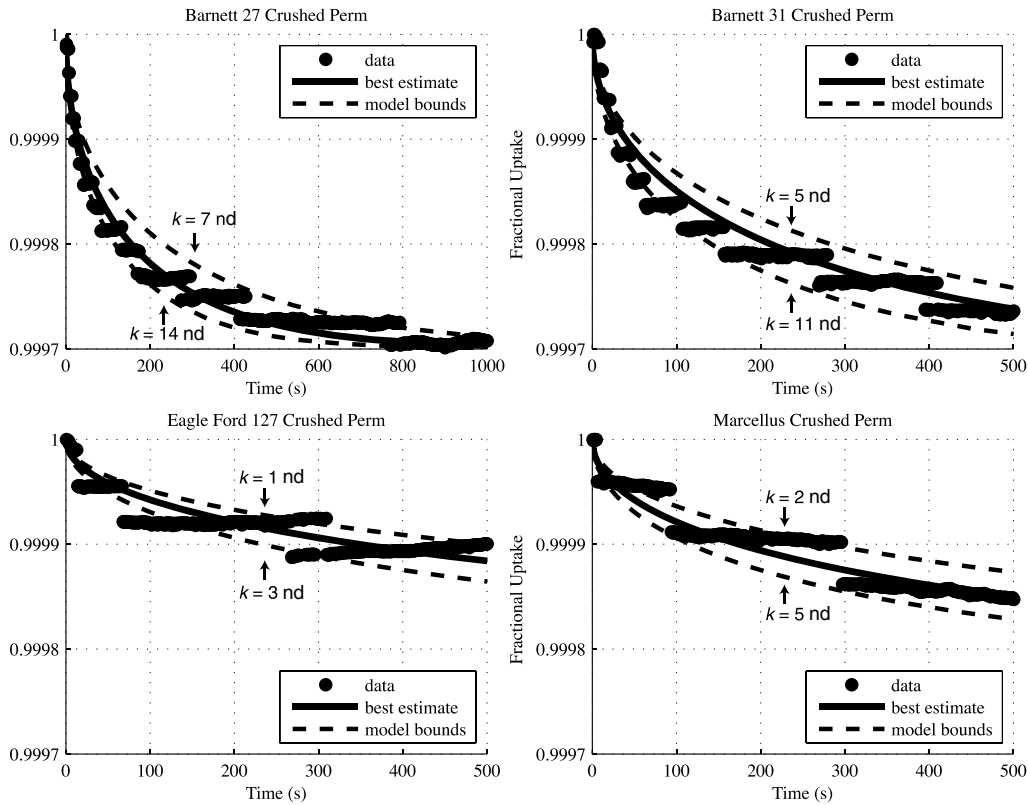


Figure 12. Lower and upper crushed permeability bounds (indicated by dashed lines bounding data) calculated using the method outlined by Cui et al. (2009). We calculate the permeability at this scale to be within the narrow range of about 1 to 10 nd. A comparison of crushed and intact permeability values is made in Figure 13.

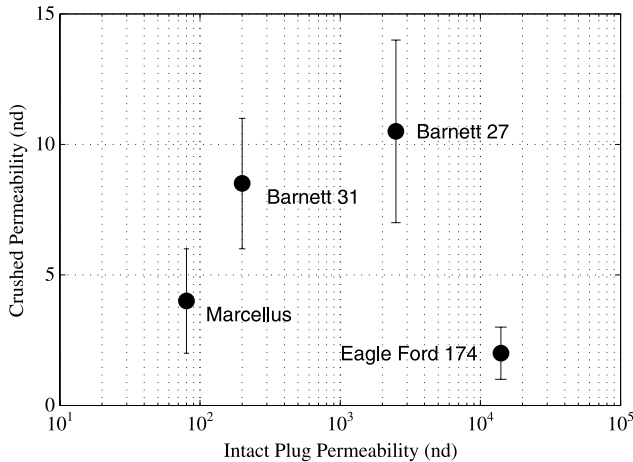


Figure 13. Crushed permeability versus intact plug permeability. Error bars indicate range of crushed permeability estimate. Plug permeability at zero effective stress was estimated by extrapolating the permeability-effective stress trends shown in Figure 8 to zero effective stress. We observe a narrow range of permeability at the particle scale (approximately 1–10 nd) regardless of the magnitude at the plug scale. In addition, we do not identify any obvious trend relating permeability at the two different scales.

the wells exists in which these samples were collected. Therefore, we can safely assume that the rock samples were not heavily saturated in oil. In addition, any hydrocarbons that were present are likely to be relatively immobile and simply acting as part of the rock. Thus, for a given sample, residual hydrocarbons would impose the same influence for all measurements and, therefore, not impact our results in any significant way.

Plug Permeability Measurements

The rate of flow of gas through the shale plugs is extremely low. Thus, minute system leaks can be an important challenge in these experiments. We were able to overcome this issue in several ways. First, leaks were minimized by keeping the number of fittings and valves to a minimum. All connections were carefully adjusted and monitored for leaks prior to experiments, including numerous pressure tests. The “leakier” side of the system was always chosen as

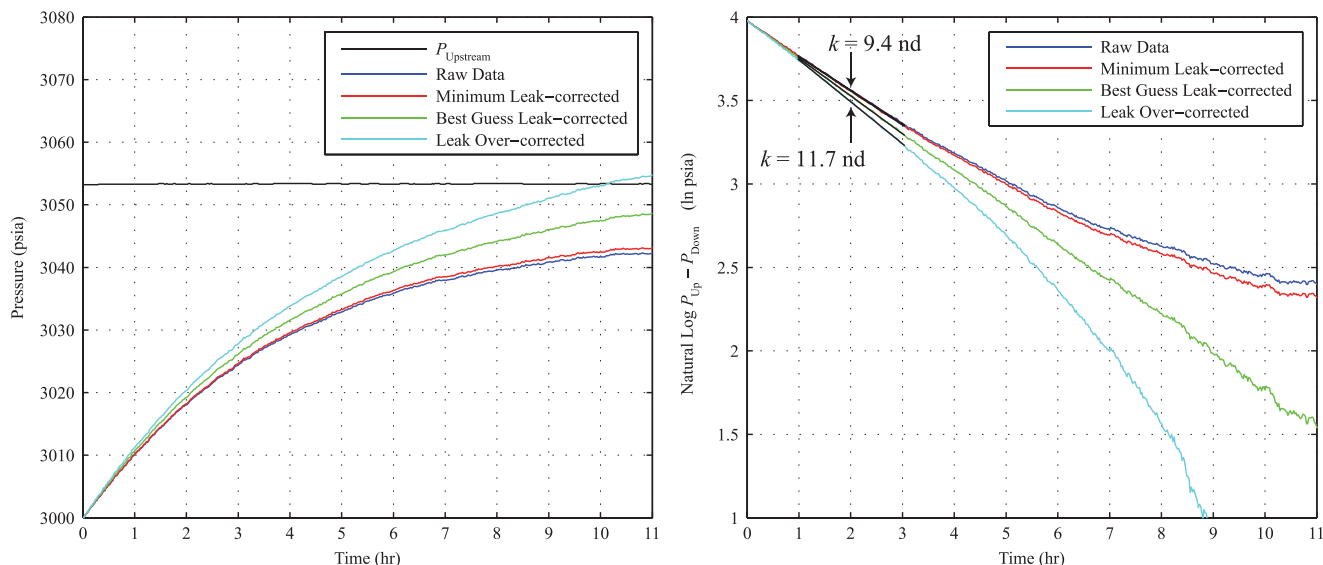


Figure 14. Left: pressure in the upstream and downstream volume of our system versus time during a permeability measurement. In addition to the raw data, minimum-leak-rate-corrected data, best-guess-leak-rate-corrected data and leak-overcorrected data are shown as well. Estimating permeability from early time data (1–3 hr) minimizes the impact of leaks and leak corrections, such that regardless of the leak correction approach, permeability lies within a narrow and acceptable range.

the upstream side and, thus, negated given our constant upstream pressure boundary condition. Typical leak rates from the downstream volume were less than 10^{-8} mol/second. Note the relatively large downstream volume we have chosen (~ 15 mL) relative to what may be typical for these experiments. Using a larger volume helps minimize the significance of leak rates on the pressure signal, albeit at the expense of longer equilibration times.

Given that setting up an experiment involves reconnecting the pore lines each time, it would not be valid to assume a leak rate measured in a calibration run to be the same leak rate occurring during our experiments. However, we believe we can safely assume a lower bound on leak rate to be our best calibration run and, therefore, correct all pressure data for this minimum rate. In Figure 14, we present an example of the data before and after the minimum-leak-rate correction, as well as curves demonstrating best-guess-leak-corrected and overcorrected data. Comparing these curves at early times (1–3 hr) and estimating permeability from each, it is apparent that leaks have a minimal impact on the data such that regardless of whether the permeability is estimated from the raw data, minimum-leak-corrected, best-guess-leak-corrected or overcorrected data, the

permeability estimate lies in a narrow range (9.4 to 11.7 nd). If permeability were estimated from later time data, however, the results would be quite different. Therefore, we chose to estimate all permeability from early time data (1–3 hr) so that the impact of leaks and leak corrections is minimized.

As discussed, great efforts were taken to minimize sources of error to the pressure vs. time data. Nevertheless, our data are not without error, and room for improvement exists. In Table 2, we summarize what we believe to be some of the key technical challenges standing in the way of higher quality data, and the approaches that we have already taken or are considering for future experiments.

In addition to minimizing error in the pressure vs. time data, several studies have suggested alternative approaches for analyzing these curves. In particular, authors have examined higher order models that might more accurately describe the combination of flow regimes acting in these rocks (Roy et al., 2003; Javadpour, 2009). Darabi et al. (2012) modified equation 6 to include slip flow and Knudsen diffusion and used a data-matching approach to arrive at a final permeability estimate. Future works might compare the results achieved using such sophisticated approaches with those attained through more traditional methods.

Table 2. Experimental Challenges, Actions that Have Been Taken to Address Those Challenges as Well as Potential Future Improvements

| Technical Challenge | Action Taken | Level of Influence | Potential Improvements |
|---|---|--------------------|--|
| Helium leaking out of upstream volume | Infinite upstream volume boundary condition (imposed using QX pump) renders leaks irrelevant on upstream side. | None | N/A |
| Helium leaking out of downstream volume and/or through jacket | Leak rate low; corrected for lowest observed. Relatively large downstream volume reduces significance of leak rate. | Low | Switch from helium to argon gas for measurements. Further reduce connections on downstream side. |
| Helium bypassing sample | Control experiment with steel plug in place of sample showed no evidence of this. | None | Repeat control experiment regularly to monitor for issues related to sample bypass. |
| Confining stress fluctuations with temperature impacting the shape of the $\Delta P(t)$ curve | Pressure data analyzed where confining pressure and temperature are stable. | Moderate | Thermal stability of system has been improved. An electronic pump could be installed to ensure confining pressure stability. |
| Nonuniform fluid properties across length of core sample | Minimized using smaller pulses at low pressures, where fluid properties vary more significantly with pressure. | Dependent on gas | Other approaches for data analysis (example, numerical simulations of pressure vs. time data). |

Crushed Permeability Measurements

Permeability experiments on crushed samples are much simpler and faster to perform, but along with this convenience carry many challenges from a data analysis standpoint. Estimates are very sensitive to both porosity and system volume measurements. We have mostly diminished this source of uncertainty using a carefully designed system with adjustable void volumes for optimal sensitivity. We have assumed that after initial gas expansion and filling of void volume, the pressure change was small enough to neglect compressibility effects. We have also assumed all particles to be spherical in shape as has been done by previous investigators. In addition, we emphasize that we report bounds on crushed-sample permeability as opposed to a single-value estimate. The resolution and sampling frequency of our pressure transducers limited our ability to more precisely constrain the shape of the pressure decay curve. Finally, despite recognizing its potential significance to flow at such low pressures, we have neglected Klinkenberg slippage effects in our analysis. Until measurement and data analysis standards are established for crushed permeability, adding complexities

like the Klinkenberg effect provide little benefit. Other authors have cited the need for establishing such standards as well (Sondergeld et al., 2010; Sinha et al., 2012).

DISCUSSION

A summary of all experiments performed and data presented thus far is presented in Table 3. We first developed permeability effective stress laws for six samples from four different shale plays. The magnitude of the Klinkenberg effect was measured for three of these six samples by making permeability measurements at relatively low pressures and separating the stress effects from slippage effects using a graphical method. Based on the magnitude of the Klinkenberg effect, we were able to make pore width estimates. Finally, four of the six samples were crushed for further permeability characterization at the particle scale.

All of our intact plug permeability measurements lay within a similar range of those presented in the literature by other authors. In the case of the Barnett Shale, we measured one sample to have a

Table 3. Summary of Experiments Performed and Data Presented in This Work

| Sample | P_p Range (psi) | C_p Range (psi) | χ | Plug Permeability at $\sigma_{\text{eff}} = 0$ (nd) | Crushed Permeability (nd) | Comments |
|----------------|----------------------|----------------------|--------|--|---------------------------------|------------------|
| Barnett 27 | 1000–4000 | 1000–4000 | 0.82 | 1200 | 10.5 | Carbonate streak |
| Barnett 31 | 1000–4000 | 1000–4000 | 0.68 | 100 | 8.0 | |
| Eagle Ford 127 | 250–4000 | 1000–4000 | 0.60 | 9000 | 2.0 | Carbonate streak |
| Eagle Ford 174 | 250–4000 | 1000–4000 | 0.40 | 15 | N/A | |
| Marcellus | 250–3000 | 1000–4000 | 0.15 | 35 | 3.5 | |
| Montney | 1000–4000 | 1000–3000 | 0.85 | 11,000 | N/A | Small crack |

permeability in the range of 60 to 160 nd depending on effective stress, whereas another contained a carbonate streak and ranged from about 0.8 to 1.8 μd . Kang et al. (2011) similarly measured the permeability of a Barnett plug to be in the range 10 to 100 nd, whereas Wang and Reed (2009) measured a plug permeability in the range of 1 to 10 μd . We measured permeability of two Eagle Ford samples: one with a permeability in the range of 5 to 40 nd and another with a carbonate streak in the range of 6 to 12 μd . Mullen (2010) described the permeability of the Eagle Ford as ranging from 1 to 800 nd. The Montney sample we characterized turned out to be very permeable (8 to 14 μd), although this was likely caused by the presence of a crack. However, note that other studies of Canadian shale samples have measured permeability in a similar range of 1 to 10 μd (Clarkson et al., 2012). Finally, we measured vertical permeability in the Marcellus to range from 20 to 60 nd.

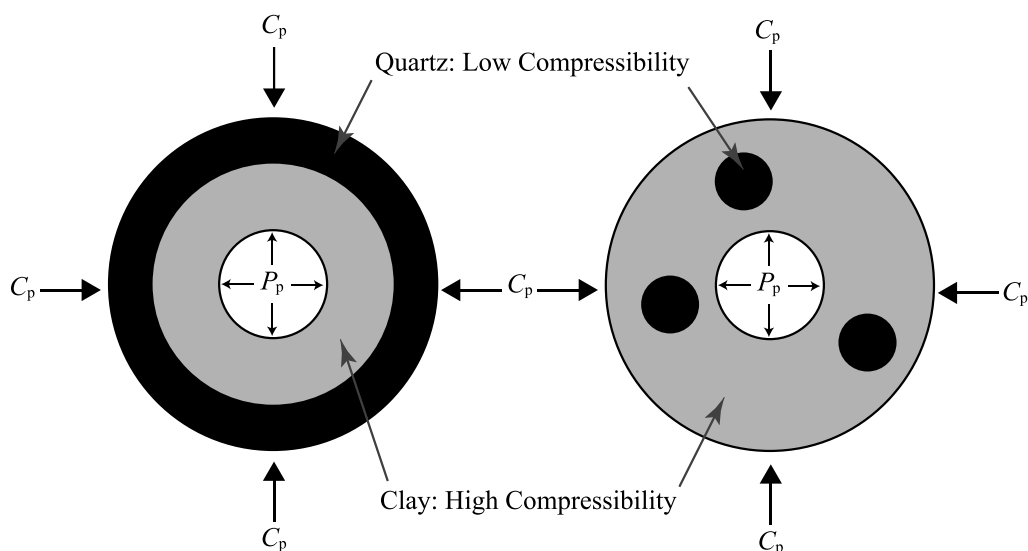
Direct comparison of our crushed permeability results with other studies is difficult because of differences in methodology and particle size. For example, Sinha et al. (2012) sent the same set of four samples to two different vendors for crushed permeability measurement. One vendor calculated permeability to be 10 to 20 nd, whereas another vendor estimated permeability to be between 100 and 1000 nd. Cluff et al. (2007) presented approximately 20 Barnett shale crushed permeability measurements with an average value of about 0.1 nd, but ranging to as low as 1 pd. Guidry et al. (1995) shares results of about 20 “black shale” crushed permeability measurements, ranging in magnitude between 1 and 1000 nd. An order-of-magnitude comparison of our

results with these studies places our estimates approximately in the middle of the range.

Our permeability effective stress experiments indicate that the matrix permeability of gas shales is likely more sensitive to changes in pore pressure than changes in confining stress, as indicated from our observation of $\chi < 1$ in all of our samples. Given these results, the model proposed by Zoback and Byerlee (1975), in which a compressible pore space exists within a stiff granular framework, must be modified for shales. Kwon et al. (2001) similarly observed $\chi < 1$ in their measurements of the Wilcox shale and proposed a model in which clays form a connected matrix and are thus similarly affected by confining pressure and pore pressure (this model is shown in Figure 15). This work seems to confirm this hypothesis. However, given our estimation of pore widths and observation of pores of a similar width within both clay and kerogen in SEM images, we believe connected flow paths to exist in kerogen as well. From a production perspective, the implications of $\chi < 1$ are positive because decreasing the pore pressure by a given amount will reduce the permeability of the shale to a lesser amount. Nevertheless, the effective stress is still increasing, and one can expect the capacity of the matrix to allow Darcy flow to decline with pore pressure during production.

Although effective stress effects narrow the aperture of flow paths and inhibit fluid flow, slip flow could offer a mechanism of transport to offset the reduced Darcy flux. In other words, as pressure decreases during production, competing processes acting on the rock matrix exist, one acting to decrease flow capacity (pore compression) and one acting to increase it (slip flow). Because we have measured

Figure 15. Left: simplified pore models developed by Zoback and Byerlee (1975) sandstone with strong stress-supporting frame (black) and high-compressibility clays (gray) lining pores (white). Right: Kwon et al. (2001) model where clay forms a connected matrix in which flow paths reside. Given our observation of $\chi < 1$ in all samples, we support the Kwon model (on the right) for shales, in which effective pore widths are similarly affected by changes in confining and pore pressure.

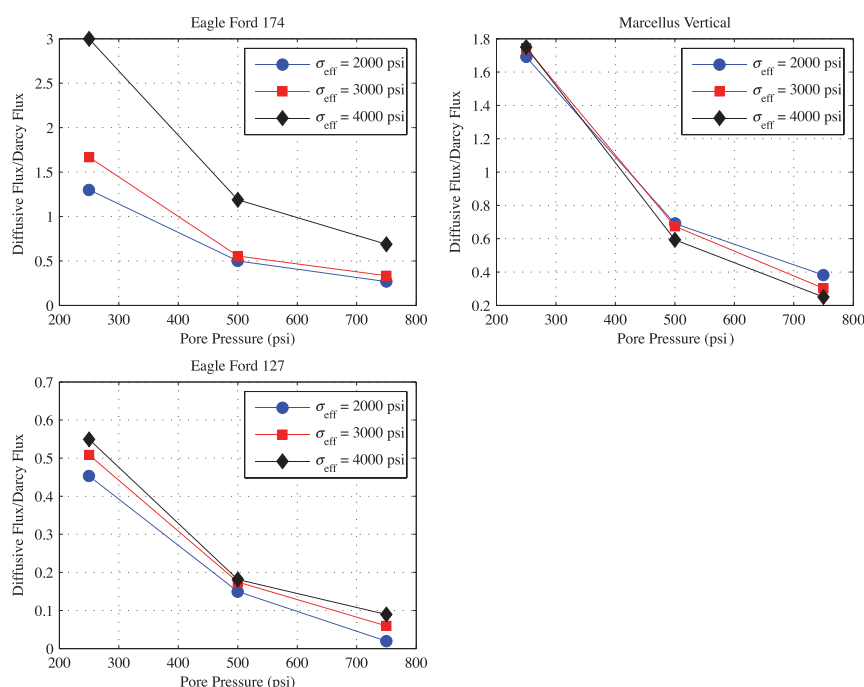


the magnitude of slip flow occurring in our samples as a function of effective stress, we can estimate how the total contribution to flow from each transport mechanism will evolve during production. These results are presented in Figure 16, in which the contribution of diffusive flux (slip flow) relative to Darcy flux is plotted as a function of pore pressure and effective stress. In the two lower permeability samples (Eagle Ford 174, and Marcellus), the ratio becomes greater than one near a pore pressure of 400 psi (2.8 MPa), indicating an important

contribution from slip flow at such conditions. In the case of the more permeable Eagle Ford 127 sample, the contribution from slip flow is less significant, although still not negligible, at pore pressures less than 400 psi (2.8 MPa).

Comparing the contribution of slip flow to total flow as a function of effective pressure, one observes an apparent relationship between this ratio and effective stress. In the case of the two Eagle Ford samples, increasing effective stress at a given pore pressure results in an increase in the relative contribution of

Figure 16. Contribution of slip flow relative to Darcy flux as a function of pore pressure and effective stress. Note in the two lower permeability samples (Eagle Ford 174 and Marcellus), the ratio becomes greater than 1 at about 400 psi (2.8 MPa). In the case of the more permeable Eagle Ford 127 sample, the contribution from slip flow is less significant but not negligible at pore pressures less than approximately 400 psi (2.8 MPa).



slip flow (likely for narrowing pores, thereby both decreasing Darcy flux and increasing Knudsen flow). In the case of the Eagle Ford 174 sample, increasing effective stress from 3000 to 4000 psi (20.7 to 27.6 MPa) seems to drastically impact this ratio for reasons that are unclear. Recall that this was the least permeable sample of the group. Finally, notice that the Marcellus vertical sample does not behave in the same way as the two Eagle Ford samples in response to increasing effective stress. More specifically, the relative contribution of slip flow to total flow appears to remain rather constant.

Note that the magnitude of slip flow will be less with methane as the flowing gas relative to helium. Given that the mean free path of helium is roughly double that of methane at the pressures studied in these experiments, it is likely that the magnitude of the slip-page effect for methane would be roughly half what we measured for helium. Although this implies less of a contribution to total flow than shown in Figure 16, it does not obviate the conclusion that slip flow may be an important contributor to total flow at low pressures. Moreover, note that in the case of methane, the potential for surface diffusion exists (Tien, 1994). Despite being an entirely different and separately occurring transport mechanism, surface diffusion would superficially be the same factor as slip flow. That is, it would allow an enhancement of fluid flow at low pressures. This additional flow mechanism may partially offset the lesser amount of slip flow in the case of methane, resulting in a similar cumulative importance of all diffusive fluxes at low pore pressure.

CONCLUSIONS

We have conducted laboratory experiments on gas shales examining the effects of confining stress and pore pressure on matrix permeability. Our results show the matrix permeability of gas shales to be more sensitive to changes in confining pressure than changes in pore pressure. In addition, data suggest that the effective permeability of the rock is significantly enhanced at very low pore pressures (<500 psi [<3.4 MPa]) because of slippage effects. By separating these effects, we are able to make standard Klinkenberg permeability plots and calculate the effective size of the flow paths within the sample and how those sizes might vary with

effective stress. Our estimates are on the order of tens of nanometers, in general agreement with SEM image observations of pores within kerogen. Finally, we calculate the relative contribution of slip flow to Darcy flow as a function of pore pressure and effective stress. We estimate a significant contribution from slip flow to total flow at pore pressures less than about 400 psi (2.8 MPa), perhaps exceeding that of Darcy flow in tighter, lower permeability rocks. We hypothesize that the increasing importance of slip flow at low pore pressures may help explain the relatively long and flat production tails observed in some shale plays (e.g., Valko and Lee, 2010).

APPENDIX 1: DERIVATION OF EFFECTIVE PORE SIZE AS A FUNCTION OF KLINKENBERG CONSTANT

Suppose we assume that the total flow is the sum of the viscous flow plus some empirical constant times the Knudsen flow (Klinkenberg made a similar assumption). We also assume a slit-shaped pore geometry. If we model the viscous flow using the Poiseuille equation, we can write the following:

$$Q = \frac{w^4}{12\mu L} \Delta P + c \frac{4}{3P} \left(\frac{2RT}{\pi M} \right)^{1/2} \frac{w^3}{L} \Delta P \quad (10)$$

where Q is the total volumetric flow rate (m^3/s), the first term is the viscous flow rate, the second is the Knudsen flow rate, c is an empirical constant, and w is the slit width. If we combine this with Darcy's Law,

$$Q = \frac{kA}{\mu L} \Delta P \quad (11)$$

and then solve for permeability, we get

$$k = \frac{w^4}{12A} + c \frac{4\mu w^3}{3PA} \left(\frac{2RT}{\pi M} \right)^{1/2} \quad (12)$$

which we can then rewrite as

$$k = \frac{w^4}{12A} \left[1 + \frac{16c\mu}{wP} \left(\frac{2RT}{\pi M} \right)^{1/2} \right] \quad (13)$$

Equation A4 has the same form as the Klinkenberg equation (equation 5). Thus, this simple model yields the following relation for the Klinkenberg constant, K_b :

$$K_b = \frac{16c\mu}{w} \left(\frac{2RT}{\pi M} \right)^{1/2} \quad (14)$$

which can easily be solved for w ,

$$w = \frac{16c\mu}{K_b} \left(\frac{2RT}{\pi M} \right)^{1/2} \quad (15)$$

providing us with a direct linkage between the empirical Klinkenberg constant and pore aperture.

APPENDIX 2: SAMPLE PROPERTIES

Mineralogy, Kerogen Analyses and Other Sample Characteristics for Sample Used in This Analysis

| | Barnett 27 | Barnett 31 | Eagle Ford 127 | Eagle Ford 174 | Marcellus | Montney |
|--------------------------------|------------|------------|-------------------|-------------------|-----------|------------|
| Depth (ft) | 8629.2 | 8640.8 | 12,771.35 | 12,845.25 | 6300 | 7614.52 |
| Depth (m) | 2630.2 | 2633.7 | 3893.70 | 3916.23 | 1920.73 | 2321.50 |
| Plug orientation | Horizontal | Horizontal | Horizontal | Horizontal | Vertical | Horizontal |
| Length (in.) | 0.95 | 0.64 | 1.50 | 0.27 | 0.32 | 1.23 |
| Length (cm) | 2.4 | 1.61 | 3.81 | 0.69 | 0.81 | 3.12 |
| TOC (%) | 3.8 | 5.3 | 1.81 | 4.4 | 1.17 | 2.04 |
| Quartz (%) | 56.7 | 51.3 | 7 | 16.4 | 38 | 42.3 |
| Plagioclase/feldspar (%) | 3.8 | 4 | 4 | 1.9 | 6 | 11.9 |
| Calcite (%) | 7.7 | 0 | 80 | 47.5 | 1 | 8.1 |
| Dolomite (%) | 1.4 | 0.4 | 1 | 0 | 1 | 9.9 |
| Pyrite (%) | 1.8 | 1.7 | 1 | 6.7 | 1 | 3.5 |
| Apatite (%) | 1 | 0 | 2 | 0.6 | 1 | 0 |
| Total clay (%) | 23.8 | 37.4 | 5 | 22.4 | 52 | 24.1 |
| S_1 (mg HC/g rock) | 4.8 | 4.4 | 2.88 | N/A | 2.06 | N/A |
| S_2 (mg HC/g rock) | 4.5 | 6.1 | 1.36 | N/A | 5.15 | N/A |
| S_3 (mg HC/g rock) | 0.3 | 0.3 | 0.54 | N/A | 0.31 | N/A |
| T_{\max} (°C) | 448 | 452 | 466 | N/A | 369 | N/A |
| HI (mg HC/g TOC) | 119 | 115 | 75 | N/A | 439 | N/A |
| OI (mg CO ₂ /g TOC) | 8 | 6 | 30 | N/A | 26 | N/A |

REFERENCES CITED

- Al-Wardy, W., and R. W. Zimmerman, 2004, Effective stress law for the permeability of clay-rich sandstones: *Journal of Geophysical Research*, v. 109, p. B04203, doi: 10.1029/2003JB002836.
- Brace, W. F., J. B. Walsh, and W. T. Frangos, 1968, Permeability of granite under high pressure: *Journal of Geophysical Research*, v. 73, p. 2225–2236, doi: 10.1029/JB073i006.p02225.
- Bustin, R. M., A. M. M. Bustin, A. Cui, D. Ross, and V. M. Pathi, 2008, Impact of shale properties on pore structure and storage characteristics: Society of Petroleum Engineers Shale Gas Production Conference, Fort Worth, Texas, USA, November 16–18, 2008, SPE 119892-MS, 28 p., doi: 10.2118/119892-MS.
- Clarkson, C. R., J. L. Jensen, P. K. Pedersen, and M. Freeman, 2012, Innovative methods for flow-unit and pore-structure analyses in a tight siltstone and shale gas reservoir: *AAPG Bulletin*, v. 96, p. 355–374.
- Cluff, R. M., K. W. Shanley, and M. A. Miller, 2007, Three things we thought we knew about shale gas but were afraid to ask (abs.): AAPG 2007 Annual Conference, Long Beach, California, accessed November 2013, <http://www.searchanddiscovery.com/abstracts/html/2007/annual/abstracts/lbCluff.htm>.
- Cui, X., A. M. M. Bustin, and R. M. Bustin, 2009, Measurements of gas permeability and diffusivity of tight reservoir rocks: Different approaches and their applications: *Geofluids*, v. 9, p. 208–223, doi: 10.1111/j.1468-8123.2009.00244.x.
- Curtis, M., R. Ambrose, C. Sondergeld, and C. S. Rai, 2010, Structural characterization of gas shales on the micro- and nano-scales: Canadian Unconventional Resources and International Petroleum Conference, Calgary, Alberta, Canada, October 19–21, 2010.
- Darabi, H., A. Ettehad, F. Javadpour, and K. Sepehrmoori, 2012, Gas flow in ultra-tight shale strata: *Journal of Fluid Mechanics*, v. 710, 641 p.
- Egermann, P., R. Lenormand, D. Longeron, and C. Zarcone, 2003, A fast and direct method of permeability measurement on drill cuttings: *Petrophysics Houston*, v. 44, p. 243–252.
- Freeman, C. M., G. J. Moridis, and T. A. Blasingame, 2011, A numerical study of microscale flow behavior in tight gas and shale gas reservoir systems: *Transport in Porous Media*, v. 90, p. 253–268, doi: 10.1007/s11242-011-9761-6.
- Ghabezloo, S., J. Sulem, S. Guédon, and F. Martineau, 2009, Effective stress law for the permeability of a limestone: *International Journal of Rock Mechanics and Mining*

- Sciences, v. 46, p. 297–306, doi: 10.1016/j.ijrmms.2008.05.006.
- Guidry, K., D. Luffel, and J. Curtis, 1995, Development of laboratory and petrophysical techniques for evaluating shale reservoirs, final report: Des Plaines, Illinois, Gas Technology Institute, GRI-95/0496, 304 p.
- Javadpour, F., 2009, Nanopores and apparent permeability of gas flow in mudrocks (shales and siltstone): *Journal of Canadian Petroleum Technology*, v. 48, p. 16–21, doi:10.2118/09-08-16-DA.
- Javadpour, F., D. Fisher, and M. Unsworth, 2007, Nanoscale gas flow in shale gas sediments: *Journal of Canadian Petroleum Technology*, v. 46, p. 55–61.
- Kang, S. M., E. Fathi, R. Ambrose, I. Akkutlu, and R. Sigal, 2011, Carbon dioxide storage capacity of organic-rich shales: *SPE Journal*, v. 16, p. 842–855.
- Klinkenberg, L. J., 1941, The permeability of porous media to liquids and gases: *Drilling and production practice*: American Petroleum Institute, p. 200–213.
- Kowalczyk, P., S. Furmaniak, P. A. Gauden, and A. P. Terzyk, 2010, Carbon dioxide adsorption-induced deformation of microporous carbons: *Journal of Physical Chemistry C*, v. 114, p. 5126–5133, doi:10.1021/jp911996h.
- Kwon, O., A. K. Kronenberg, A. F. Gangi, and B. Johnson, 2001, Permeability of Wilcox Shale and its effective pressure law: *Journal of Geophysical Research*, v. 106, p. 19,339–19,353, doi:10.1029/2001JB000273.
- Loucks, R. G., R. M. Reed, S. C. Ruppel, and D. M. Jarvie, 2009, Morphology, genesis, and distribution of nanometer-scale pores in siliceous mudstones of the Mississippian Barnett Shale: *Journal of Sedimentary Research*, v. 79, p. 848–861, doi:10.2110/jsr.2009.092.
- Luffel, D. L., and F. K. Guidry, 1989, Core analysis results, comprehensive study wells, Devonian shales: Houston, Gas Research Institute, GRI Topical Report, 129 p.
- Luffel, D. L., and C. W. Hopkins, 1993, Matrix permeability measurement of gas productive shales: Society of Petroleum Engineers Annual Technical Conference and Exhibition, SPE 26633, p. 261–270.
- Mullen, J., 2010, Petrophysical characterization of the Eagle Ford Shale in south Texas: Canadian Unconventional Resources and International Petroleum Conference, Calgary, Alberta, Canada, October 19–21, 2010, SPE 138145-MS, 19 p., doi: 10.2118/138145-MS.
- Nur, A., and J. D. Byerlee, 1971, An exact effective stress law for elastic deformation of rock with fluids: *Journal of Geophysical Research*, v. 76, p. 6414–6419, doi: 10.1029/JB076i026p06414.
- Profice, S., D. Lasseux, Y. Jannot, N. Jebara, and G. Hamon, 2011, Permeability, porosity and Klinkenberg coefficient determination on crushed porous media: International Symposium of the Society of Core Analysts, Austin, Texas, September 18–21, 2011, SCA2010-32, 12 p.
- Roy, S., R. Raju, H. F. Chuang, B. A. Cruden, and M. Meyyappan, 2003, Modeling gas flow through microchannels and nanopores: *Journal of Applied Physics*, v. 93, p. 4870–4879, doi: 10.1063/1.1559936.
- Sinha, S., E. Braun, Q. Passey, S. Leonardi, A. Wood, III, T. Zirkle, and R. Kudva, 2012, Advances in measurement standards and flow properties measurements for tight rocks such as shales: Society of Petroleum Engineers/European Association of Geoscientists and Engineers European Unconventional Resources Conference and Exhibition, Beijing, China, June 8–10, 2010, SPE 152257-MS, 13 p., doi: 10.2118/152257-MS.
- Soeder, D. J., 1988, Porosity and permeability of eastern Devonian gas shale: *Society of Petroleum Engineers Formation Evaluation*, v. 3, no. 1, p. 116–124.
- Sondergeld, C. H., R. J. Ambrose, C. S. Rai, and J. Moncrieff, 2010, Micro-structural studies of gas shales: Society of Petroleum Engineers Unconventional Gas Conference, Pittsburg, Pennsylvania, February 23–25, 2010, SPE 131771-MS, 17 p., doi: 10.2118/131771-MS.
- Thorntenson, D. C., and D. W. Pollock, 1989, Gas transport in unsaturated zones: multicomponent systems and adequacy of Fick's laws: *Water Resources Research*, v. 25, p. 477–507.
- Tien, C., 1994, Adsorption calculations and modeling: Newton, Massachusetts, Butterworth-Heinemann, 244 p.
- Valko, P., and W. Lee, 2010, A better way to forecast production from unconventional gas wells: Society of Petroleum Engineers Annual Technical Conference and Exhibition, Florence, Italy, September 19–22, 2010, SPE 134231-MS, 16 p., doi: 10.2118/134231-MS.
- Walls, J., and A. Nur, 1979, Pore pressure and confining pressure dependence of permeability in sandstone: 7th Formation Evaluation Symposium, Canadian Well Logging Society, Calgary, Alberta, Canada, October 1979.
- Wang, F. P., and R. M. Reed, 2009, Pore networks and fluid flow in gas shales: Society of Petroleum Engineers Annual Technical Conference and Exhibition, New Orleans, Louisiana, October 4–7, 2009, SPE 124253-MS, 8 p., doi: 10.2118/124253-MS.
- Warpinski, N. R., and L. W. Teufel, 1992, Determination of the effective-stress law for permeability and deformation in low-permeability rocks: *Society of Petroleum Engineers Formation Evaluation*, v. 7, p. 123–131.
- Yang, Y., and A. C. Aplin, 2010, A permeability–porosity relationship for mudstones: *Marine and Petroleum Geology*, v. 27, p. 1692–1697.
- Zoback, M. D., and J. D. Byerlee, 1975, Permeability and effective stress: *AAPG Bulletin*, v. 59, p. 154–158.